The Cryosphere

Discussions

Open Access

EGU

1 **InSAR monitoring of Arctic land fast sea ice deformation using**

2 **L-band ALOS-2, C-band Radarsat-2 and Sentinel-1**

3 Zhaohua Chen[1], Benoit Montpetit[1], Sarah Banks[1], Lori White[1], Amir Behnamian[1], Jason Duffe[1],

4 Jon Pasher[1]

5 Science and Technology Branch, Environment and Climate Change Canada, Ottawa, Ontario, K1S 5B6, Canada

6 *Correspondence to*: Zhaohua Chen (zhaohua.chen@canada.ca)

7

8 **Abstract.** Arctic amplification is accelerating changes in sea ice regimes in the Canadian Arctic with later freeze-up

9 and earlier melt events, adversely affecting Arctic wildlife and communities that depend on the stability of the sea ice

10 conditions. To monitor both the rate and impact of such change, there is a need to accurately measure sea ice

11 deformation, an important component for understanding ice motion and polar climate. This paper presents

12 Interferometric Synthetic Aperture Radar (InSAR) monitoring of Arctic landfast sea ice deformation as a result of

13 thickness changes measured from ice draft and surface height using C-band Radarsat-2, Sentinel-1 and L-band ALOS-

14 2. The small baseline subset (SBAS) approach was explored to process time series observations for retrieval of

15 temporal deformation changes over the winter. Sea ice deformation (subsidence and uplift in the range of -32-57 cm)

16 detected from satellite SAR data in Cambridge Bay, Nunavut, Canada during the winter of 2018-2019 was found to

17 be in a range of values corresponding to the ice draft growth (30-62 cm) measured from an in-situ ice profiler. The

18 trends of InSAR observations from Sentinel-1 were also consistent with ice surface height changes along two ground

19 tracks detected from ICESat-2. SAR backscatter from Sentinel-1 also corresponded to the surface height with strong

20 correlation coefficient (0.49-0.83). High coherence over ice from C-band was maintained over a shorter acquisition

21 interval than L-band due to temporal decorrelation.

22

23

24 **1 Introduction**

25 Arctic ice has been thinning and retreating due to global warming in recent years (Tucker et al. 2001; Perovich et al.,

26 2008; Kwok et al., 2009; Wadhams, 2012). Given the vast sea ice extent and increasing commercial interest in the

27 Arctic, it is important to map sea ice changes (Dawson et al., 2020). SAR satellite imagery are used routinely to

28 identify and map sea ice changes due to its weather-independent capability (Zakhvatkina et al., 2019). Several C-band

29 SAR satellites are also used to provide operational products of sea ice types, extent and concentration due to the

30 availability of large amount of imagery (Arkett et al., 2006; Tivy, et al., 2011; Zakhvatkina et al., 2019). With

31 increasing data available from other SAR sensors, X- and L-band have also been found to provide complementary

32    information for sea ice identification (Drinkwater et al., 1991; Eriksson et al., 2010; Casey et al. 2016; Johansson et

33    al., 2018).

34    In addition to information on sea ice extent, types, and concentration, measurements of sea ice thickness and

35    kinematics are critical for understanding the impacts of the Arctic climate change (Zwally et al., 2008; Kwok, 2010).

36    Measurements of these parameters using satellite images are challenging because monitoring dynamic sea ice

37    processes requires high spatial and temporal resolution data (Kwok, 2010). A direct measurement of ice thickness can

38    be made through ice draft observations from in-situ sensors. Ice draft is a measurement of the ice thickness below the

39    waterline and may be used as a proxy for total ice thickness (Fisse et al., 2008). Currently, sea ice thickness is not

40    directly measured from space, but indirect measurements including surface height variations and freeboard have been

41    used to provide information related to thickness (Petty et al., 2016; Cafarella et al., 2019). Traditional methods like

42    ice core drilling and sonar or radar systems are used to obtain ice information below the water line, making them both

43    complex and resource intensive to implement over a large area. By comparison, satellite-based methods are cost-

44    effective and have demonstrated the potential for ice surface height measurements over large areas. Surface height

45    information can be measured by the radar altimeter from the Cryosat-2 satellite (Bouffard et al., 2018; Tilling et al.,

46    2018) or the lidar altimeter from Ice, Cloud, and land Elevation Satellite (ICESat-1 and ICESat-2) (Kwok et al., 2019).

47    Compared to the 369-day repeat cycle of Cryosat-2, ICESat-2 has a 91-day orbit cycle, providing higher temporal

48    frequency data for monitoring Arctic sea ice since its launch in 2018 (Kwok et al., 2019). ICESat-2 measurements

49    theoretically represent the vertical height of ice/snow surface above sea level. With close to 1-2 cm accuracy, surface

50    height measurements from laser pulses bouncing off the ice surface can be very important for studying ice conditions

51    in the Arctic (Kwok et al., 2016; Kwok et al., 2019). However, measurements from these altimeters are only point

52    data along the orbit, limiting their spatial coverage.

53    Surface height changes may also be measured indirectly by Interferometric Synthetic Aperture Radar (InSAR), a

54    technique that measures the line-of-sight (LOS) motion of a target based on the phase differences between two SAR

55    images. In fact, ice deformation has been investigated using this method near the Beaufort Sea coast (Meyer et al.,

56    2011; Dammann et al., 2016; Dammann et al., 2018a; Dammann et al., 2018b) and the Baltic sea coast (Dammert et

57    al., 1998; Berg et al., 2015; Marbouti et al., 2017). It is believed that most of the InSAR phase change over a coherent

58    area are the results of vertical or horizontal movements of the sea ice (Dammert et al., 1998; Meyer et al., 2011; Berg

59    et al., 2015; Dammann et al., 2018a). The deformation is an important component of ice motion. It is attributed to

60    thermal expansion and contraction or dynamic deformation (e.g., compression of the ice driven by winds, sea level

61    tilt, currents, or internal ice stress (Dammann et al., 2016; Marbouti et al., 2017). Aided with inverse modeling, InSAR

62    may be used to determine ice deformation modes (Dammann et al., 2016), rates (Meyer et al., 2011), dynamics (e.g.,

63    associated stress and fracture patterns) (Dammert et al., 1998; Berg et al., 2015; Marbouti et al., 2017; Dammann et

64    al., 2018b; Dammann et al., 2019), and topography (Dammann et al., 2018b; Dierking et al., 2017). However, it is

65    difficult to verify InSAR measurements of ice deformation due to the cost associated with the installation of equipment

66    for in-situ measurements and the difficulty of accessing ice away from the shore.

67  InSAR measurements of sea ice deformation can be affected by several factors including coherence, frequency, sea

68  ice thickness and others (e.g. wetness, salinity). Interferometric information is useful only if the phase differences are

69  from coherent areas. Coherence (value ranges from 0 to 1) is used to describe the quality of an interferogram which

70  contains phase changes. Higher coherence values indicate higher phase correlation and less noise in interferometric

71  phase. Usually, targets that remain unchanged during the time interval of two image acquisitions have high coherence.

72  On the other hand, low coherence values can be a result of temporal decorrelation, where there is little to no correlation

73  observed among groups of pixels observed at the same location, through time. This can be a result of either significant

74  motion occurring between acquisitions (measured relative to the radar wavelength) and/or due to a low temporal

75  frequency of acquisitions. Notably, temporal decorrelation can be significant in areas dominated by ice, especially

76  floating ice, due to relatively quick horizontal movements as a result of wind/currents/waves (Berg et al., 2015;

77  Dammann et al., 2016; Marbouti et al., 2017). Though generally speaking, for most natural surfaces, the longer the

78  time interval between acquisitions, the lower the coherence. Loss of coherence is also dependent on the wavelength.

79  Decorrelation is more pronounced at shorter wavelengths such as X-band (2.5-4 cm), and C- (4-8 cm) than longer

80  wavelengths such as L-band (15-30 cm). Many InSAR studies confirm improved coherence in L-band SAR data

81  (Rosen et al., 2000; Dammann et al., 2016; Meyer et al., 2011). Wavelength also affects InSAR results because it

82  impacts how incident microwaves interact with the snow/ice surface and ice volume (Kwok, 2010; Berg et al., 2015;

83  Dammann et al., 2016). Thus, the sensitivity of SAR to sea ice deformation is dependent on the penetration depth of

84  a respective wavelength (Dierking and Busche, 2006; Dierking and Dall, 2007; Johansson et al., 2018). Longer

85  wavelength microwaves can penetrate deeper than shorter wavelength microwaves (Johansson et al., 2018). InSAR

86  coherence is generally higher and more stable over stationary landfast ice than drifting ice (Dammann et al., 2016;

87  Dierking et al., 2017; Marbouti et al., 2017; Dammann et al., 2018a; Dammann et al., 2018b). As a result, current

88  efforts to monitor sea ice deformation using satellite data have therefore been mainly limited to landfast ice (Dammert

89  et al., 1998; Meyer et al., 2011; Berg et al., 2015). Landfast sea ice is an essential element of Arctic coastal sea ice

90  systems, and its stability is critical for transportation and activities using ice as a platform (Dammann et al., 2016).

91  Understanding the response of SAR signals to changes in surface height above the sea level and thickness changes

92  below the sea level can help determine the patterns and sources of deformation, a critical first step to better

93  investigating the impacts of climate change on sea ice. To calculate the ice deformation over a certain period with

94  time series SAR images, small baseline subset (SBAS) (Berardino et al., 2002; Usai, 2003) may be applied. The SBAS

95  method can connect interferograms spanning in different time intervals and generate cumulative measurements of

96  movements while limiting and correcting effects from temporal decorrelation , atmosphere and topography (Berardino

97  et al., 2002; Usai, 2003; Samsonov et al., 2014; Chen et al., 2016; Chen etal., 2020). Once the deformation is derived,

98  validation of InSAR results is important. The validation of InSAR results can help improve the generation of products

99  related to ice stability, thickness and ice conditions. With frequent SAR acquisitions, InSAR derived measurements

100  may provide the information with increased spatial and temporal coverage that is not available from the in-situ ice

101  profiler and ICESat-2. InSAR deformation is the projection of the three-dimensional ice movement along the LOS

102  direction, containing both horizontal and vertical information. Assuming that fast ice does not move with wind and

103  sea current, and the vertical deformation over stationary fast ice is the dominant movement due to changes of ice

104    thickness, InSAR LOS deformation over coherent fast ice may reflect surface height variations measured by ICESat-
105    2 as well as the ice draft measured from the in-situ ice profiler, which could be verified via correlation analyses. From
106    this perspective, we investigated InSAR derived deformation information observed from SAR satellites and compared
107    with surface height changes measured from satellite lidar altimeter and ice draft measured from the in-situ ice profiler
108    in Cambridge Bay, Nunavut, Canada. The surface deformation measurements from SAR sensors including L-band
109    ALOS-2, C-band Radarsat-2 and Sentinel-1 were generated using InSAR techniques. In this paper, we evaluated the
110    sensitivity of SAR backscatter to sea ice surface height changes, investigated changes and differences in coherence
111    between L- and C- band SAR data over arctic sea ice, and assessed how InSAR observations correlate to surface
112    height variations and ice draft growth.

113

114

115    **2 Study area and data**

116    Cambridge Bayis located on Victoria Island, Nunavut, Canada. It is directly connected to the Arctic Ocean and is
117    partially covered by ice for most of the year. This study monitored the sea ice covering the Northwest Passage through
118    the Arctic Ocean between Dease Strait (located on the left side of Cambridge Bay) and Queen Maud Gulf (located on
119    the right side of Cambridge Bay) (Figure 1). During winter months, the entire area is covered by landfast first year ice
120    (FYI) which varies in thickness depending on the time of year (Figure 2). Some multi-year ice (MYI) may flow from
121    Victoria Strait to the east into the Queen Maud Gulf but regional climate charts available from the Canadian Ice
122    Service Data Archive (CISDA) (Tivy et al., 2011) showed that the dominant ice type was FYI with varying surface
123    roughness and thickness in the study area (Figure 2).
124    For this area, ice draft information was provided by an upward looking sonar water ice profiler (SWIP), deployed by
125    Ocean Networks Canada. The ice profiler uses acoustics to measure the ice thickness, known as ice draft, and is
126    mounted on the ocean floor at a depth of 6 m near the Cambridge Bay dock (Ocean Networks Canada, 2019) (Figure
127    1).  A review of the observatory data of ice draft from previous years indicates that ice was formed on 15 October, 7
128    October, 1 October, and 8 October in 2016, 2017, 2018 and 2019, respectively. The ice melted on 29 June, 13 July,
129    and 29 July in 2017, 2018 and 2019, respectively. The ice thickness reached to a maximum of 1.62 m on May 29,
130    2017, 1.55 m on June 11, 2018, and 1.85 m on June 11, 2019 respectively.
131    A total of six Radarsat-2 scenes of Fine Quad-Pol mode (FQ13) were collected during December 2018-May 2019
132    (Table 1 and Figure 1). Each image was acquired in the ascending orbit and was quad-polarized (HH, HV, VH, and
133    VV). A total of 15 Sentinel-1 scenes of Interferometric Wide (IW) mode were collected during November 2018-April
134    2019. The IW datasets in descending orbit were dual-polarized (HH and HV). A total of six ALOS-2 scenes of HBQR
135    mode were acquired during January-April 2019. The HBQR datasets of the high-sensitive mode were also acquired
136    in the descending orbit and were quad-polarized (HH, HV, VH, and VV). InSAR coherence from HH polarization has
137    been proven to be higher and more stable than other polarizations in studying targets with low backscatter such as
138    permafrost (Chen et al., 2016; Samsonov et al., 2016) and some wetlands types (Chen et al., 2020). Preliminary studies
139    showed that HH polarization usually returned stronger backscatter which meant higher signal to noise ratio (SNR),

140   and was thus advantageous over other polarizations in monitoring low backscatter areas such as ice and water.
141   Therefore, HH polarization was chosen for ice monitoring in this study. The seasonal melting and freezing of ice
142   causes changes in surface temperature and salinity, so all images were acquired during December-May because ice
143   conditions were more stable. A Canadian Digital Elevation Data (CDED) of 30 m spatial resolution was used to
144   provide elevation information for image co-registration and topographic correction in InSAR processing. The
145   elevations in the study area including land and ocean range between 0 and 90 m above mean sea level according to
146   CDED.

147   The location of the Arctic Station building in Cambridge Bay was chosen as a reference for InSAR measurements
148   (RP). Four locations over the sea ice (P1, P2, P3, P4), representing different ice conditions, corresponding to water
149   depths of 10 m deep near harbor to more than 70 m deep in the strait (Canadian Hydrographic Service, 2007), were
150   selected to investigate the ice deformation using InSAR. Consistent coherence was also maintained at these locations
151   in interferograms from both ALOS-2 and Sentinel-1 images (Figure 3 and Figure 7). P1 was located in an area with a
152   water depth of 10-20 m, P2 in 40-60 m, P3 in 60-70 m, and P4 in 40-50 m (Figure 1). These locations were also 5-10
153   km away from the shore. No location near the harbor was selected for InSAR monitoring because of its small size and
154   proximity to land, making it easily affected by the resampling and filtering process. One location on the land near the
155   sea was chosen for studying the movements of the land (P5).

156   The along-track sea ice surface heights were available from the ATL07 product from NASA's second-generation
157   spaceborne lidar mission ICESat-2, with 17 m footprint, and 0.7 m along-track spacing. Each acquisition contains
158   profiles of sea surface/ice height segments from three beam-pairs. Each pair consists of a strong and a weak beam,
159   with pulse energies of the strong beams that are four times those of the weak (Kwok et al., 2019). In this study we
160   only used surface heights from three strong beam tracks at each acquisition time assuming that the measurements from
161   strong beams were more reliable than weak beams.

162

163   Table 1. SAR data used for the InSAR analysis.

| Sensor | Mode | Resolution (range x azimuth) | Incidence angles (degrees) | Repeat cycle (days) | Number of scenes acquired 2018-2019 |
|---|---|---|---|---|---|
| Radarsat-2 | FQ13 | 16.5 x 14.9 | 33 | 24 | 6 |
| ALOS-2 | HBQR | 4.3 x 5.1 | 39 | 14 | 6 |
| Sentinel-1 | IW | 2.7 x 22 | 33.4 | 12 | 15 |

164

165

166   **3 Methods**

167    In this study backscatter, coherence and deformation analyses were completed. First, SAR backscatter intensity of
168    different modes and sensors was compared with surface height variations from ICESat-2 data. Second, coherence
169    variations over ice from interferograms generated with different acquisition intervals on different months were
170    assessed. Third, the response of InSAR measurements to the surface height and ice draft was studied using time series
171    analysis.

172    Traditional differential InSAR (D-InSAR) procedures including co-registration, interferogram generation and phase
173    unwrapping were applied to each dataset with GAMMA software (Werner et al., 2000). First, co-registration was
174    applied to align and resample all images from one orbit (same sensor, polarization, and incidence angle) to a reference
175    image. Multi-looking and resampling were applied to reduce speckle effects and to improve coherence estimation.
176    Then, all possible InSAR pairs which were acquired within 90 days and perpendicular baseline less than 400 m were
177    used to generate differential interferograms. Atmospheric correction was also applied to each interferogram based on
178    the split-spectrum method which separates the ionospheric and the non-dispersive phase terms using spectral sub-band
179    images (Wegmueller, et al., 2018). The phase noise of an interferogram was reduced using an adaptive phase filter
180    (Goldstein and Werner, 1998), and then coherence and phase changes were estimated. The interferogram was
181    unwrapped to estimate the ice movements along the LOS using the Minimum Cost Flow algorithm (Costantini, 1998).
182    Backscatter variability can be used to study the ice types and conditions (Kwok and Cunningham, 1994; Casey et al.
183    2016). The backscattering coefficient was calculated to describe the interaction between incident microwaves with
184    sea ice. Its variation is related to wavelength, polarization, incidence angles, and ice properties such as surface
185    roughness, internal structure and dielectric properties. For the backscatter analysis, a radiometric calibration was
186    applied, and intensity values were converted to decibels (dB in $\sigma°$). Backscattering coefficients ($\sigma°$) were generated
187    along the ICESat-2 laser tracks to evaluate the SAR response to the surface height changes. During the original surface
188    height generation for ICESat-2 ATL07 product, the height segments were sampled to have overlap with each other
189    along the laser track. Hence, along-track height estimates were not independent because they included photons from
190    an earlier segment (Kwok et al., 2019). Surface height points also had higher spatial resolution than ALOS-2, Radarsat-
191    2 and Sentinel-1. Therefore, we generated the moving average in order to resample the surface height estimates from
192    ATL07 products to a resolution matching SAR data. $\sigma°$ values of SAR imagery and surface height measurements from
193    ICESat-2 acquired at the closest available dates were compared, assuming ice conditions remained the same between
194    the acquisitions. Correlation between SAR $\sigma°$ values and surface heights was calculated as well. By acquiring data
195    with similar incidence angles from ALOS-2, Radarsat-2 and Sentinel-1, backscatter differences in images at the same
196    time were expected to be largely related to the wavelength.

197       Once interferograms were generated, a threshold of 0.3 was used to identify coherent and non-coherent areas. Only
198    those areas which maintained high coherence (>0.3) were kept and correctly unwrapped for the next SBAS analysis.
199    Assuming no significant movement at RP (Figure 1) during the study period, the deformation change was set to zero
200    at RP. Then, a deformation map with respect to the reference pixel was computed to provide relevant information only
201    to those pixels with high coherence.

202    By exploiting all available SAR acquisitions, using interferograms generated from the D-InSAR technique with short
203    spatial and temporal baselines, the SBAS technique was applied to the to calculate the temporal evolution of
204    deformation. In the analysis, the Singular-Value Decomposition (SVD) algorithm was employed to achieve the
205    minimum-norm least squares solution and to extract meaningful deformation information at any time interval. Finally,
206    time-series cumulative deformation was achieved. In this analysis, negative values in InSAR deformation indicated
207    subsidence, while positive values in deformation indicated uplift. Then, cumulative ice draft growth was also
208    calculated from the measurements from the ice profiler and compared with cumulative deformations from InSAR
209    observations. Since time series surface heights were not available, the responses of InSAR deformation to the surface
210    height variation over a certain winter period were evaluated.

211

212

### 4 Results

### 4.1 Observations of backscatter responding to surface height

215    Data from the SAR sensors showed that the HH $\sigma°$ values of landfast ice were generally low. For example, $\sigma°$ values
216    of ALOS-2 and Sentinel-1 from P1-P4 varied in the range of (-29)-(-22) dB and (-35)-(-26) dB respectively, and only
217    varied within 5 dB at the same location during January-April, indicating that ice conditions were stable. Based on the
218    comparison of backscatter from three SAR sensors with surface height, backscatter from Sentinel-1 responded better
219    to surface height variations than ALOS-2 and Radarsat-2. The correlation between SAR $\sigma°$ values and surface height
220    are given in Table 2.

221    For comparison with ALOS-2 backscatter, ground tracks from only two orbits of ICESat-2 were covered by ALOS-2
222    data. Two orbits were flown on 2019/1/30 and 2019/2/25 respectively. Scenes acquired on 2019/1/31 and 2019/2/28
223    were the two ALOS-2 data with the nearest dates corresponding to the ICESat-2 data. The $\sigma°$ values of each ALOS-2
224    image in the HH polarization were compared with the surface height measurements along the ground tracks from three
225    strong beams of each orbit of ICESat-2 (Figure 3). Results showed that surface heights along the tracks of ICESat-2
226    acquired on 2019/01/30 showed less variation than that of 2019/2/25. SAR intensity from the HH polarization of L-
227    band ALOS-2 did not always show similar pattern as that of surface height (Figure 4). Ice surface heights varied in
228    the range (-3)-(3) cm along the tracks from all three strong beams of ISCESat-2, and SAR intensity from ALOS-2
229    acquired on 2019/1/31 varied in the range (-27)-(-19) dB along the same tracks (Figure 4A-C). In particular, both the
230    surface height and SAR intensity showed little variation along the track of 3L (Figure 4C). In contrast, ice surface
231    heights along the tracks of three beams of 2019/2/25 varied by (-3)-(16) cm, while SAR intensity from ALOS-2
232    acquired on 2019/2/28 varied in the range (-28)-(-18) dB (Figure 4D-F). The pattern of $\sigma°$ values exhibited a greater
233    range and corresponded better to observed surface height values on 2019/2/25, which were also more variable (19
234    cm). Relative to 23 cm wavelength from ALOS-2, all measurements of surface roughness were well below a detectable
235    level, and therefore backscatter was low and not very responsive to the surface height changes. The correlation
236    between ALOS-2 $\sigma°$ values and surface heights varied in each track of two dates with correlation coefficients range

237    from -0.1 to 0.78 (Table 2). Although track of 3L on 2019/1/31 provided the highest correlation coefficient (r=0.78),

238    the sample size was the smallest among six tracks.

239

240    Table 2. Correlation between ice surface height (from ICESat-2) and SAR backscattering coefficient (σ° in dB) (*

241    only used the surface height larger than 0.3 m for correlation analysis).

| Date | ICESat-2 track | ALOS-2 | Radarsat-2 | Sentinel-1 |
|---|---|---|---|---|
| 2018-12-25 | 1R | NA | 0.07 | NA |
|  | 2R | NA | -0.63 | NA |
|  | 3R | NA | -0.1 | NA |
| 2019-01-23 | 1L * | NA | NA | 0.68 |
|  | 2L * | NA | NA | 0.68 |
|  | 3L | NA | NA | 0.54 |
| 2019-01-30 | 1L | 0.6 | NA | NA |
|  | 2L | -0.1 | NA | NA |
|  | 3L | 0.78 | NA | NA |
| 2019-02-25 | 1L | 0.2 | 0.23 | NA |
|  | 2L | 0.68 | 0.03 | NA |
|  | 3L | 0.51 | 0.5 | NA |
| 2019-02-28 | 1L | NA | NA | 0.83 |
|  | 2L | NA | NA | 0.49 |
|  | 3L | NA | NA | 0.55 |

242

243    For comparison with Radarsat-2 backscatter, ground tracks from only two orbits of ICESat-2 were covered by

244    Radarsat-2 data. Two ICESat-2 orbits were acquired on 2018/12/25 and 2019/2/25 respectively. Radarsat-2 FQ13

245    scenes acquired on 2018/12/22 and 2019/2/8 were the two datasets with the nearest dates corresponding to the ICESat-

246    2 data. The σ° values of each Radarsat-2 image in the HH polarization were compared with surface heights along the

247    ground tracks from three strong beams of each orbit of ICESat-2 (Figure 5). Due to the relatively small footprint of

248    Radarsat-2, only a small area of overlap between Radarsat-2 and ICESat-2 was available for comparison. SAR

249    intensity from the HH polarization of C-band Radarsat-2 FQ13 did not show similar patterns to surface heights (Figure

250    6). Ice surface heights varied in the range 35-61 cm along the tracks acquired on 2018/12/25, and SAR intensity

251    acquired on 2018/12/22 varied in the range 6-13 dB along the same track. However, SAR backscatter fluctuated in

252    the opposite direction to surface height in many areas. Ice surface heights varied in the range (-2)-(17) cm along the

253    tracks acquired on 2019/02/25, and SAR intensity on 2019/02/8 varied in the range 2-13 dB along these tracks.  In

254    general, for the ground tracks along the Radarsat-2 coverage, backscatter was not responsive to surface height changes.

255    The correlation between Radarsat-2 σ° values and surface heights varied in each track of two dates with correlation

256    coefficients range from (-0.63) to (0.5) (Table 2). The sample numbers of all six tracks were very small, especially

257    along tracks of 1R and 3L. Radarsat-2 backscatter was much higher than ALOS-2 and Sentinel-1 images because ice

258    look up table (LUT) was applied to all Radarsat-2 scenes over the sea by default.

259    Sentinel-1 has very large coverage, so it covered more ICESat-2 tracks than ALOS-2 and Radarsat-2. σ° values of

260    Sentinel-1 IW of 2019/1/24 were compared with the surface heights of ICESat-2 of 2019/1/23 along the tracks of 1L,

261    2L and 3L, and σ° values of Sentinel-1 IW of 2019/3/1 were compared with the surface heights of ICESat-2 of

262    2019/2/28 along the tracks of 1L, 2L and 3L (Figure 7). Results indicated that the surface height and the SAR intensity

263    from Sentinel-1 along these tracks had large variations on both dates. For example, the surface height variation was

264    about 58 cm on the tracks of 2019/01/23 and about 45 cm on tracks of 2019/02/25. SAR backscatter appeared to be

265    highly correlated with ice surface height at many point locations (Figure 8). SAR backscatter was stronger in areas

266    where surface height was high, and SAR backscatter was weaker in the area when surface height was low. In particular,

267    ice surface heights varied in the range 0-58 cm along the tracks acquired on 2019/01/23, while SAR intensity acquired

268    on 2019/01/24 varied in the range (-35)-(-27) dB in the same areas (Figure 8A-C). Ice surface heights varied in the

269    range 31-76 cm along the tracks on 2019/02/28, and SAR intensity on 2019/3/1 varied in the range (-34)-(-27) dB

270    along the same tracks (Figure 8D-F). In general, surface heights along two ground tracks were as high as 80 cm above

271    sea level, and varied in range of 30-50 cm. The correlation between Sentinel-1 σ° values and surface heights were

272    generally strong in each track of two dates with correlation coefficients range from 0.49 to 0.83 (Table 2). The sample

273    numbers of all six tracks were very large, especially along tracks of 1R and 3L. It was found that σ° values may have

274    different patterns in places with surface height above 30 cm and below 30 cm. For example, the correlation between

275    σ° values and surface heights along track 1L on 2019/01/23 were 0.68 and 0.43 in places above 30 cm and below 30

276    cm respectively though the correlation was only -0.26 when combined.

277

### 4.2 Observations of coherence change over time

279    Coherence from C- band Radarsat-2 and Sentinel-1 and L-band ALOS-2 InSAR pairs were generated for the period

280    of December 2018 - May 2019. Coherence from interferograms generated over short and long acquisition intervals

281    was compared. In general, high coherence was observed over sea ice from L-band as early as in January, but high

282    coherence from C-band was only measured from mid-February. It was also found that coherence from L-band could

283    be maintained over a longer time period than C-band. For example, all InSAR interferogram pairs from ALOS-2 data

284    acquired from January to April 2019 produced good coherence. However, coherence was highest in interferograms

285    with a 14-day interval, and decreased gradually as time spans between acquisitions increased (i.e. from 28, 42, 56, 70

286    and 84-day intervals). Almost all ice areas remained coherent in the interferograms of 14 and 28-day intervals, while

287    only 60% of this area remained coherent in the interferograms with 84-day interval. Both the harbor and Queen Maud

288    Gulf area were coherent in most interferograms. With stable coherent ice areas, the SBAS analysis of time series

289    ALOS-2 interferograms was conducted for cumulative deformation estimates.

290    Radarsat-2 FQ13 coverage was smaller than ALOS-2 and Sentinel-1 coverage, thus the sea ice area observed was

291    limited to the Cambridge Bay harbor and nearby areas only. Coherence in interferograms of 48-day interval was

292    generally very poor compared to those of 24-day interval. Coherence values were low from interferograms generated

293    using images acquired during December and early February. It was observed that only harbor areas were coherent

294    from the interferograms of 2018/12/22_2019/1/15 and 2019/1/15_2019/2/8 among the images acquired before mid-

295    February. Coherence was greatly improved in the interferograms generated using images acquired between March

296    and mid-May. As such, the majority of ice areas were coherent from the interferograms of 2019/3/28/_2019/4/21 and

297    2019/4/21_2019/5/15/. SBAS analysis was not applied to Radarsat-2 data due to limited number of quality

298    interferograms.

299    Low coherence was observed in the interferograms generated from November Sentinel-1 images, and similar to

300    observations from Radarsat-2 images, coherence was also poor from December to January. Starting in January,

301    coherence was observed from ice in the middle of the Dease Strait but limited to small patches. Coherent areas were

302    also observed near Hurd Islands, an area beneath Dease Strait, protected from the influence of wind, waves and ocean

303    currents. Starting at mid-February, high coherence was observed across Dease Strait and area near Queen Maud Gulf

304    although there were still some areas including harbor with low coherence. From mid-March until the end of April, the

305    whole area including the harbor, Dease Strait and Queen Maud Gulf was highly coherent in Sentinel-1 12-day

306    interferograms, though half of the area lost coherence in interferograms with a 24-day interval. During this time high

307    coherence was observed in some areas over a 36-day period, though represented few, small and sporadically

308    distributed sites. Compared to the interferograms from ALOS-2 data, interferograms from Sentinel-1 before mid-

309    February were patchy and inconsistent. Therefore, only InSAR pairs from mid-February to April could be used for

310    the SBAS analysis.

311    Based on our observations, it was found that coherence over sea ice were strongly affected by temporal baselines. As

312    such, interferograms from longer time intervals, in particular from C-band Radarsat-2 data, may not be suitable for

313    ice deformation monitoring due to low coherence, and a small temporal baseline subset is preferred for ice deformation

314    estimates.

315

316    **4.3 Characterizing the response of InSAR deformation to ice draft growth**

317    The cumulative estimates of deformation in the LOS direction from SBAS analysis of both ALOS-2 and Sentinel-1 at

318    four locations were compared with ice draft measurements. No cumulative estimates were available from Radarsat-2

319    due to a lack of sufficient interferograms for SBAS analysis, instead, differential estimates of deformation at only two

320    locations were compared with ice draft. All InSAR measurements were calibrated as changes relative to the RP.

321    Results from ALOS-2 (Figure 9A) during January-April 2019 and results from Sentinel-1 (Figure 9B) during

322    February-April 2019 both indicated that the land location P5 experienced only a slight fluctuation in position during

323    the study period. InSAR results from both sensors indicated that the general subsidence trends in deformation were

324    the same at P1 and P4 locations (Figure 9). More than 30 cm deformation at P4 was detected from both ALOS-2 and

325  Sentinel-1 observations. However, the deformation trends measured from two sensors were opposite at P2 and P3

326  locations.

327  According to the ice profiler at the dock location of Cambridge Bay, ice draft began to accumulate from 2018/10/13,

328  became 40 cm thick by the end of October, and peaked at 1.85 m on 2019/6/8, then decreased until it was completely

329  melted on 2019/7/2 (Figure 10). Results indicated that ALOS-2 InSAR observations at four locations showed different

330  movements as a response to a 62 cm ice growth during January 17-April 11, 2019, the ALOS-2 observation period.

331  For example, cumulative deformation from ALOS-2 InSAR indicated an uplift of 57 and 52 cm at P2 and P3, but a

332  subsidence of 6 and 31 cm at P1 and P4 (Figure 9A). In particular, a downward deformation of about 24 cm occurred

333  during February 28-March 28 at P4. At the same time, Sentinel-1 InSAR observation at all four locations showed a

334  trend of subsidence in response to an increase of 30 cm of ice draft during February 17-April 6, 2019, the Sentinel-1

335  observation period. For example, cumulative deformation from Sentinel-1 InSAR indicated a downward motion of

336  2.5, 18, 8 and 32 cm at P1, P2, P3 and P4, respectively (Figure 9B). It was observed that ice at the P3 location

337  experienced a downward movement during March 1-March 25, then an uplift movement during March 25-April 6,

338  2019. D-InSAR results from three pairs of Radarsat-2 acquired from February to May measured a cumulative uplift

339  of 7 cm at P1, but a subsidence of 13 cm at P4 in response to the ice draft growth of 53 cm during the same time period

340  (Table 3). The subsidence trend at P4 detected by Radarsat-2 was consistent to that observed from ALOS-2 and

341  Sentinel-1 data. However, the deformation magnitude detected from Radarsat-2 was much less than that from ALOS-

342  2 and Sentinel-1.

343

344  Table 3. D-InSAR measurements at location P1 and P4 using Radarsat-2 FQ13 data vs ice draft measurements from

345  the ice profiler located close to RF.

|  | InSAR (P1) | InSAR (P4) | Ice Draft |
|---|---|---|---|
| 2019/02/08-2019/03/28 | 0.02 | -0.01 | 0.33 |
| 2019/03/28-2019/04/21 | 0.03 | -0.04 | 0.12 |
| 2019/04/21-2019/05/15 | 0.02 | -0.08 | 0.08 |

346

347  **4.4 Characterizing the response of InSAR deformation to surface height variation**

348  In order to understand how InSAR derived measurements of deformation corresponded to surface height changes, ice

349  surface height changes derived from ICESat-2 during the SAR observation period were analyzed. Although ICESat-

350  2's repeat cycle is 91 days, no two acquisitions from the same orbit were available within the 91-day cycle, however,

351  there were two acquisitions from the same path for a 182-day interval. The same ground track was scanned on

352  2018/10/24 and 2019/4/24 individually. Another track in the vicinity of these two acquisitions, with a distance of 345

353  m, was acquired on 2019/1/23. However, among three strong beams from each acquisition, only two beams from the

354  acquisition of 2019/1/23 were close to the two beams of the acquisition of 2018/10/24 and 2019/4/24. Therefore, the

355    surface height variations from these three dates along two ground tracks were compared. In the analysis, line 1R of

356    2018/10/24, line 2L of 2019/01/23 and 1L of 2019/04/24 were simply considered as one ground track spatially for

357    comparison (referred to as Line 1) (Figure 11 A-C).  Line 2R of 2018/10/24, line 3L of 2019/01/23 and 2L of

358    2019/04/24 were considered as the other ground track spatially for comparison (referred to as Line 2) (Figure 11 D-

359    F).

360    Surface heights were plotted against latitude for comparison as the general flight direction was north to south. It was

361    found that surface heights along Line 1 and Line 2 were generally below mean sea level on 2018/10/24, mostly in the

362    range of (-25)-(-10) cm (Figure 11A for Line 1 and Figure 11D for Line 2), then increased above sea level on

363    2019/01/23, mostly in the range of 30-60 cm (Figure 11B for Line 1 and Figure 11E for Line 2), and remained above

364    sea level on 2019/04/24, mostly in the range of 5-40 cm (Figure 11C for Line 1 and Figure 11F for Line 2). The

365    variations of heights in three dates from these two tracks suggested that the surface height was negative or below sea

366    level at the beginning of ice forming, then increased to at least 30 cm above sea level in mid-January, then decreased

367    to some extent in April, but remained at least 5 cm above sea level. However, surface heights showed much greater

368    variations at different locations along the track over a short distance in January and April than in October.

369    InSAR deformation is the measurement of change along the LOS projection. It contains components of both horizontal

370    and vertical movements of sea ice. Line 1 and Line 2 from ICESat-2 were located far from Cambridge Bay, they were

371    only covered by Sentinel-1 imagery. Due to the small coverage, no pairs of the same or close orbit from an ICESat-2

372    acquisition were covered by ALOS-2 and Radarsat-2 during the study period. Therefore, the InSAR deformation

373    measurements from ALOS-2 and Radarsat-2 were not compared with surface height changes. Cumulative deformation

374    estimates from Sentinel-1 images during 2019/2/17-2019/4/6 were compared with the ICESat-2 surface height

375    changes from 2019/1/23 and 2019/4/24 (Figure 12). For this comparison, the surface height changes at each sample

376    point between two close orbits along Line 1 and Line 2 were calculated. Specifically, the surface height differences

377    of Line 1 were calculated by subtracting the heights of 2L of 2019/1/23 from that of 1L from 2019/4/24 (the closest

378    ground tracks during the ICESat-2 flight at two dates). Similarly, the surface height differences of Line 2 were

379    calculated by subtracting the heights of 3L of 2019/1/23 from that of 2L from 2019/4/24. Moving average of height

380    measurements at a distance similar to the resolution of Sentinel-1 SBAS product of 40 m was used. Similar patterns

381    of surface height changes were found in Line 1 and Line 2. InSAR measurements in most locations along track Line

382    1 consistently measured subsidence which was consistent with a decrease in surface heights, however, at locations

383    between latitude 68.67-68.7 degrees, the InSAR measurements indicated a slight uplift. It was found that the

384    magnitudes of InSAR deformation along these two tracks were smaller than surface height changes. For example,

385    surface height changes ranged from (-35)-(-13) cm, but InSAR only reflected the changes that ranged from (-8)-1 cm

386    along the same track.

387

388    **5 Discussion**

389  There is limited information that can be used to validate InSAR measurements of ice deformation in the Arctic ocean.
390  In this study, we investigated how InSAR deformation measurements from L-band ALOS-2, and C-band Radarsat-2
391  and Sentinel-1 corresponded with the ice draft measured from an in-situ ice profiler, as well as surface heights
392  measured from ICESat-2. We also examined the response of backscatter variations to surface height changes along
393  the ICESat-2 ground tracks and evaluated the coherence changes during the winter season. Deformation magnitudes
394  in some locations from ALOS-2 and Sentinel-1 were found to be in the same range of ice draft growth measured from
395  one location. Spatial and temporal patterns of Sentinel-1 SAR signal were generally consistent with surface height
396  changes. However, variations between the InSAR observations and measurements from ice profiler and ICESat-2
397  remained. The variations may be attributed to many factors including sensor characteristics (e.g., wavelength, repeat
398  cycle), and ice surface conditions (e.g., snow cover, salinity, surface height, thickness, roughness, stability, types, air
399  bubble concentration, and deformation) (Kwok and Cunningham, 1994; Eriksson et al., 2010; Dierking et al., 2017;
400  Cafarella et al., 2019) in addition to coherence loss from temporal decorrelation.

401  Results showed that the temporal variability of backscatter from landfast ice (first-year) was relatively low in
402  Cambridge Bay. Low variability of backscatter has also been observed from landfast ice (multi-year) in Beaufort Sea
403  in winter (Kwok and Cunningham, 1994; Steffen and Heinrichs, 2001). Throughout most time of the winter, sea ice
404  near Cambridge Bay is covered by snow. Given the fact that the snow depth in Cambridge Bay only reached to a
405  maximum of 8 cm during April-May (Howell et al., 2016), it is not likely to have had a significant influence on
406  backscatter, especially at C- and L-band backscatter due to their penetration capacity (Kwok and Cunningham, 1994;
407  Kwok, 2010).

408  Our analysis indicated that temporal changes in Sentinel-1 backscatter values corresponded to changes in surface
409  heights measured along two ground tracks of ICESat-2. In some cases, ice surface height measured from ICESat-2
410  can have uncertainties due to the snow cover (Kwok, 2010), however this is not expected to have had a significant
411  impact here due to low snow depth. In previous studies, backscatter from C-band Radarsat-2 and L-band ALOS-2
412  were found to be correlated to the FYI surface roughness measured from airborne laser scanner, and backscatter
413  increased with larger surface roughness (Cafarella et al., 2019). Low surface heights from ICESat-2 were reported to
414  correspond to low backscatter in ice leads and floes (Kwok et al., 2019). In this study, it was found that variation of
415  SAR backscatter from Sentinel-1 corresponded to changes of surface height from 0-76 cm, as generally, higher ice
416  surfaces corresponded to the higher SAR backscatter. However, such a pattern was not obvious between backscatter
417  from C-band Radarsat-2. With very similar incidence angles from both C-band SAR sensors (Table 1), similar results
418  were anticipated. Longer acquisition interval between Radarsat-2 and ICESat-2 may have contributed to the low
419  correlation. Comparing to only 1-2 days of difference in acquisitions between ICESat-2 and SAR data from ALOS-2
420  and Sentinel-2, there were 17 days difference in ICESat-2 and Radarsat-2 acquisition dates. As such, ice conditions
421  may have changed during such period. We believe the low responses to surface height changes from the backscatter
422  of ALOS-2 data and Radarsat-2 data could also be due to the low surface height and less variation along the available
423  tracks covered by data from those two sensors. Especially, for ALOS-2 data with a 23 cm wavelength, surface height
424  variations less than 10 cm would not have impacted backscatter. Thus, it is likely that backscatter over ice from L-

The Cryosphere
Discussions

425    band data may not correspond to the true ice surface due to strong penetration into the ice and snow (Dierking et al.,
426    2017). Only a small number of samples along the surface height track were used for comparison to the Radarsat-2
427    data due to their small coverage, which might have also contributed to these results. Further correlation analysis of
428    backscatter correspondence with surface height is needed.

429    The pattern and density of interferogram fringes describe the deformation type and rate, with frequent fringes
430    indicating a higher density of phase changes and greater deformation. Generally, higher fringe density indicates
431    unstable ice conditions (Dammann et al., 2019), and parallel fringes indicate strong lateral movement. Parallel and
432    dense fringes generated over the majority ice area before February in this study therefore indicated that strong lateral
433    deformation was dominant, which corresponded to the rapid ice growth observed from the ice draft measurement
434    during October-January (Figure 10). The existence of both the parallel and circular fringes from time series of
435    interferograms from three sensors indicated that there were both lateral and vertical motion over the landfast ice in the
436    study area. Circular and less dense fringes were observed over the majority of the ice area starting in February (from
437    January with ALOS-2) also indicating that vertical deformation (uplift or depression) was dominant. Decreasing fringe
438    density as ice thickens over the winter has been reported before (Dammann et al., 2016), while others have also used
439    fringe densities in general to study the stability conditions of ice (Dammann et al., 2016; Dammann et al., 2019). In
440    those studies, dense fringe areas were considered unstable. One of the differences between ALOS-2 interferograms
441    and Sentinel-1 interferograms was the fringes. In this study, ALOS-2 interferograms from January were considered
442    reliable for deformation analysis, however, Sentinel-1 interferograms were only reliable starting from mid-February.
443    Sentinel-1 InSAR interferograms from data collected before February showed parallel and dense fringes. Both ice
444    draft and surface height are measures of vertical changes of ice conditions, therefore, assuming that InSAR
445    measurements were from stable ice, this mainly corresponded to vertical deformation and could be related to vertical
446    height changes of landfast ice. However, InSAR phase near the dock where the ice profiler located measured little
447    change, meaning that the ice was frozen to the sea floor. As such, no direct link between the InSAR measurement and
448    ice draft at this location was made. Sentinel-1 interferograms generated from images acquired before mid-February
449    were not used to provide information related to vertical height changes.
450    Temporal decorrelation over ice was observed from C-band Radarsat-2 and Sentinel-1 in this study. Coherence from
451    C-band only lasted within a 24-day interval compared to L-band ALOS-2 data, which maintained coherence over an
452    84-day interval. This can be explained by the penetration depth of different wavelengths. With a stronger penetration
453    depth at L-band, the SAR signal is more sensitive to internal ice structures which are more stable in landfast sea ice
454    compared to C-band which is more sensitive to its surface structures (Howell et al., 2018). It was found that the
455    coherence from all sensors over ice was high near the harbor and along the coast where ice attached to the coastline
456    or sea floor, then decreased toward the open ocean. InSAR coherence was generally poor from the images acquired
457    before January. Similar observations of lower correlation over sea ice from C- and X- band compared to L-band were
458    also reported in other studies (Meyer et al., 2011; Dammann et al., 2018). Poor coherence over ice before January was
459    probably caused by unstable ice condition and mobile ice. The coherence was lost when the magnitude of movement
460    was large relative to the SAR wavelength and the shift between the two acquisitions changed the ice surface,
461    consequently, the interferograms could not be generated using C-band data before January.

462 Some local uplift and subsidence were observed in both SBAS analysis of ALOS-2 and Sentinel-1 InSAR data. As
463 InSAR only measures the LOS component of the three-dimensional deformation, actual ice deformation may not be
464 well represented in the study area. Also, deformation trends from one dataset may not be consistent between datasets.
465 For example, at P2 and P4 uplift was detected from ALOS-2, and as subsidence from Sentinel-1, although similar
466 subsidence trends were detected at two other locations at P1 and P4 from both ALOS-2 and Sentinel-1. Such a
467 difference may be caused by sensitivity from different wavelengths and differences in acquisition dates. In general,
468 the deformation measured from both ALOS-2 and Sentinel-1 was found to be within the same magnitude and range
469 of ice draft growth. For example, a maximum deformation of 57 cm was detected from ALOS-2 corresponding to a
470 62 cm ice draft growth during the same period. Similarly, a maximum deformation of 32 cm was detected from
471 Sentinel-1 corresponding to 30 cm ice draft growth during the same period. Unfortunately, no in-situ deformation
472 information was available to validate the InSAR results at different locations.

473 Landfast ice can often grow and cover a large area (Dammann et al., 2019). The results from this study showed that
474 the harbor area had near-zero phase change during the winter because of the ice anchored to the floor, which
475 distinguished it from the area further into the ocean. Large areas with coherence and various fringe density in the study
476 area also demonstrated the possibility of ice extent and stability mapping using InSAR which has been applied
477 elsewhere (Meyer et al., 2011; Dammann et al., 2018; Dammann et al., 2019). The pattern and density of the fringes
478 may be used to infer different stages of landfast ice. With the approach demonstrated in this paper, observations from
479 frequent SAR acquisitions showed promise for more reliable and consistent results with the in-situ measurements and
480 other available products. Studying ice stability and deformation using InSAR may be a viable solution for the Arctic
481 communities.

482
483

484 **6 Conclusions**

485 In this paper, the potential of InSAR to observe landfast ice deformation in the Arctic ocean was investigated using
486 C-band Radarsat-2 and Sentinel-1 and L-band ALOS-2 satellite data. SBAS approach was applied to generate the time
487 series deformation information. InSAR measurements were compared with both the ice draft measured from an in-
488 situ ice profiler and surface height measured from ICESat-2 satellite in order to understand the response of vertical
489 ice deformation to ice thickness changes. Circular fringes were observed over sea ice during January-April and may
490 represent vertical deformation corresponding to steady ice growth. Results indicated that uplift and subsidence patterns
491 observed from ALOS-2 varied in different locations, and the magnitudes of deformation were in the range (-31)-57
492 cm comparing to 62 cm ice draft growth during the same period. Subsidence observed from Sentinel-1 were in the
493 range (-32)-(-2.5) cm comparing to 30 cm ice draft growth. The trends of InSAR deformation from Sentinel-1 were
494 also consistent with the ice surface height changes detected from ICESat-2 along two ground tracks. L-band ALOS-2
495 achieved higher coherence over longer acquisition intervals compared to C-band Radarsat-2 and Sentinel-1 due to
496 temporal decorrelation. The challenge of temporal coherence loss could be resolved with higher temporal revisits of
497 new modern SAR sensors such as the RADARSAT Constellation Mission launched in June of 2019. SAR backscatter

498    from Sentinel-1 was found to be sensitive to the surface height changes along the ground track of ICESat-2 with
499    correlation coefficients in the range 0.49-0.83. However, correlations between SAR backscatter and surface height
500    varied and were not strong from the Radarsat-2 and ALOS-2 possibly due to limited data samples covering area with
501    little surface roughness. Results indicated that InSAR data with a high temporal revisit shows promise for investigating
502    the Arctic sea ice deformation over a large area; however, more data is needed to validate the satellite monitoring of
503    sea ice thickness changes.

504

505    **Data availability.** Sentinel-1 data can be obtained free of charge from the Copernicus Open Access Hub
506    (https://scihub.copernicus.eu/, last access: 2 October 2019). Ice draft data from Cambridge Bay, Nunavut, can be
507    obtained from Ocean Networks Canada (http://www.oceannetworks.ca, last access: 1 December 2019). ICESat-2 data
508    can be obtained from National Snow and Ice Data Center (https://nsidc.org/data/icesat-2, last access: 10 September
509    2019). The ALOS-2 data were obtained under a scientific license (see Acknowledgements) for an approved proposal
510    submitted to JAXA. The Radarsat-2 data were obtained from Canadian Space Agency. Both ALOS-2 and Radarsat-2
511    data are not publicly accessible.

512

513    **Author contributions.** ZC conducted the interferometric processing and analysis and drafted the initial manuscript.
514    BM provided critical expertise related to sea ice interpretation and analysis. JD and JP managed the project. All co-
515    authors provided valuable recommendations, editing and corrections for the final manuscript.

516

517    **Competing interests.** The authors declare no conflict of interest.

518

519    **Acknowledgements**

525

526    **References**

527
528    Arkett, M., Flett, D., Abreu, R. D., & Gillespie, C.: Sea Ice Type and Open Water Discrimination for Operational
529          Ice Monitoring with RADARSAT-2. *2006 IEEE International Symposium on Geoscience and Remote
530          Sensing*, pp. 1631-1634. Denver, 2006.

531    Berardino, P., Fornaro, G., Lanari, R., & Sansosti, E.: A new algorithm for surface deformation monitoring based on
532          small baseline differential SAR interferograms. *IEEE Transactions on Geoscience and Remote Sensing, 40*,
533          2375-2383. doi:10.1109/TGRS.2002.803792, 2002.

534 Berg, A., Dammert, P. B., & Eriksson, L. E.: X-Band Interferometric SAR Observations of Baltic Fast Ice. *IEEE*
535     *Transactions on Geoscience and Remote Sensing, 53*, 1248-1256, 2015.

536 Bouffard, J.; Webb, E.; Scagliola, M.; Garcia-Mondéjar, A.; Baker, S.; Brockley, D.; Gaudelli, J.; Muir, A.; Hall, A.;
537     Mannan, R.; Roca, M.; Fornari, M.; Féménias, P. & Parrinello, T.: CryoSat instrument performance and ice
538     product quality status, *Advances in Space Research, 62*, 1526 – 1548, 2018.

539 Cafarella, S. M., Scharien, R., Geldsetzer, T., Howell, S., Haas, C., Segal, R., & Nasonova, S.: Estimation of Level
540     and Deformed First-Year Sea Ice Surface Roughness in the Canadian Arctic Archipelago from C- and L-
541     Band Synthetic Aperture Radar. *Canadian Journal of Remote Sensing, 45*, 457-475.
542     doi:10.1080/07038992.2019.1647102, 2019.

543 Canadian Hydrographic Service: Approaches to/Approches à Cambridge Bay, CHS Nautical Chart CHS7750, scale
544     1:15000. http://www.charts.gc.ca/images/charts-cartes/chart-thumbnails/7750_1_web.png, last access: 25
545     July 2020.

546 Casey, J. A., Howell, S. E., Tivy, A., & Haas, C.: Separability of sea ice types from wide swath C- and L-band
547     synthetic aperture radar imagery acquired during the melt season. *Remote Sensing of Environment, 174*,
548     314-328. doi:https://doi.org/10.1016/j.rse.2015.12.021, 2016.

549 Chen, Z., English, J., & Adlakha, P.: InSAR Monitoring of Alaska Highway Instability in Permafrost Regions Near
550     Beaver Creek, Yukon. *Proceedings of Offshore Technology Conference.* St. John's Newfoundland and
551     Labrador, Canada: Offshore Technology Conference. doi:10.4043/27454-MS, 2016.

552 Chen, Z., White, L., Banks, S., Behnamian, A., Montpetit, B., Pasher, J., Jason, D., Bernard, D.: Characterizing
553     marsh wetlands in the Great Lakes Basin with C-band InSAR observations. *Remote Sensing of
554     Environment, 242*, 111750. doi:https://doi.org/10.1016/j.rse.2020.111750, 2020.

555 Costantini, M.: A novel phase unwrapping method based on network programming. *IEEE Transactions on
556     Geoscience and Remote Sensing, 36*, 813-821. doi:10.1109/36.673674, 1998.

557 Dammann, D. O., Eicken, H., Mahoney, A. R., Saiet, E., Meyer, F. J., & George, J. C.: Traversing Sea Ice—Linking
558     Surface Roughness and Ice Trafficability Through SAR Polarimetry and Interferometry. *IEEE Journal of
559     Selected Topics in Applied Earth Observations and Remote Sensing, 11*, 416-433, 2018a.

560 Dammann, D. O., Eicken, H., Meyer, F. J., & Mahoney, A. R.: Assessing small-scale deformation and stability of
561     landfast sea ice on seasonal timescales through L-band SAR interferometry and inverse modeling. *Remote
562     Sensing of Environment, 187*, 492-504. doi:https://doi.org/10.1016/j.rse.2016.10.032, 2016.

563 Dammann, D. O., Eriksson, L. E., Mahoney, A. R., Eicken, H., & Meyer, F. J.: Mapping pan-Arctic landfast sea ice
564     stability using Sentinel-1 interferometry. *The Cryosphere, 13*, 557–577. doi:10.5194/tc-13-557-2019, 2019.

565 Dammann, D. O., Eriksson, L. E., Mahoney, A. R., Stevens, C. W., Van der Sanden, J., Eicken, H., . . . Tweedie, C.
566     E.: Mapping Arctic Bottomfast Sea Ice Using SAR Interferometry. *Remote Sensing, 10*.
567     doi:10.3390/rs10050720, 2018b.

568 Dammert, P. B. G.; Lepparanta, M. & Askne, J.: SAR interferometry over Baltic Sea ice, *International Journal of
569     Remote Sensing, Taylor & Francis, 19*, 3019-3037, 1998.

570 Dawson, J., Carter, N., van Luijk, N., Parker, C., Weber, M., Cook, A., . . . Provencher, J.: Infusing Inuit and local
571     knowledge into the Low Impact Shipping Corridors: An adaptation to increased shipping activity and
572     climate change in Arctic Canada. *Environmental Science & Policy, 105*, 19-36.
573     doi:https://doi.org/10.1016/j.envsci.2019.11.013, 2020.

574    Dierking, W., & Busche, T.: Sea ice monitoring by L-band SAR: an assessment based on literature and comparisons
575            of JERS-1 and ERS-1 imagery. *IEEE Transactions on Geoscience and Remote Sensing, 44*, 957-970.
576            doi:10.1109/TGRS.2005.861745, 2006.

577    Dierking, W. & Dall, J.: Sea-ice deformation state from Synthetic Aperture Radar imagery - part I: comparison of C-
578            and L-band and different polarization, *IEEE Transactions on Geoscience and Remote Sensing, 45*, 3610-
579            3622, 2007.

580    Dierking, W., Lang, O., & Busche, T.: Sea ice local surface topography from single-pass satellite InSAR
581            measurements: a feasibility study. *The Cryosphere, 11*, 1967–1985. doi:10.5194/tc-11-1967-2017, 2017.

582    Drinkwater, M. R., Kwok, R., Winebrenner, D. P., & Rignot, E.: Multifrequency polarimetric synthetic aperture
583            radar observations of sea ice. *Journal of Geophysical Research: Oceans, 96*, 20679-20698.
584            doi:10.1029/91JC01915, 1991.

585    Eriksson, L. E., Borenäs, K., Dierking, W., Berg, A., Santoro, M., Pemberton, P., . . . Karlson, B.: Evaluation of new
586            spaceborne SAR sensors for sea-ice monitoring in the Baltic Sea. *Canadian Journal of Remote Sensing, 36*,
587            S56-S73. doi:10.5589/m10-020, 2010.

588    Fissel, D. B., Marko, J. R., & Melling, H.: Advances in upward looking sonar technology for studying the processes
589            of change in Arctic Ocean ice climate. *Journal of Operational Oceanography, 1*, 9-18.
590            doi:10.1080/1755876X.2008.11081884, 2008.

591    Goldstein, R. M., & Werner, C. L.: Radar interferogram filtering for geophysical applications. *Geophysical
592            Research Letters, 25*, 4035–4038. doi:10.1029/1998GL900033, 1998.

593    Howell, S. E., Komarov, A. S., Dabboor, M., Montpetit, B., Brady, M., Scharien, R. K., . . . Yackel, J. J.: Comparing
594            L- and C-band synthetic aperture radar estimates of sea ice motion over different ice regimes. *Remote
595            Sensing of Environment, 204*, 380-391. doi:https://doi.org/10.1016/j.rse.2017.10.017, 2018.

596    Howell, S. E., Laliberté, F., Kwok, R., Derksen, C., & King, J.: Landfast ice thickness in the Canadian Arctic
597            Archipelago from observations and models. *The Cryosphere, 10*, 1463–1475. doi:10.5194/tc-10-1463-
598            2016, 2016.

599    Johansson, A. M., Brekke, C., Spreen, G., & King, J. A.: X-, C-, and L-band SAR signatures of newly formed sea
600            ice in Arctic leads during winter and spring. *Remote Sensing of Environment, 204*, 162-180.
601            doi:https://doi.org/10.1016/j.rse.2017.10.032, 2018.

602    Kwok, R.: Satellite remote sensing of sea-ice thickness and kinematics: a review. *Journal of Glaciology, 56*, 1129–
603            1140. doi:10.3189/002214311796406167, 2010.

604    Kwok, R., & Cunningham, G. F.: Backscatter characteristics of the winter ice cover in the Beaufort Sea. *Journal of
605            Geophysical Research: Oceans, 99*, 7787-7802. doi:10.1029/94JC00169, 1994.

606    Kwok, R., Cunningham, G. F., Hoffmann, J., & Markus, T.: Testing the ice-water discrimination and freeboard
607            retrieval algorithms for the ICESat-2 mission. *Remote Sensing of Environment, 183*, 13-25.
608            doi:https://doi.org/10.1016/j.rse.2016.05.011, 2016.

609    Kwok, R., Cunningham, G. F., Wensnahan, M., Rigor, I., Zwally, H. J., & Yi, D.: Thinning and volume loss of the
610            Arctic Ocean sea ice cover: 2003–2008. *Journal of Geophysical Research: Oceans, 114*.
611            doi:10.1029/2009JC005312, 2009.

612    Kwok, R., Markus, T., Kurtz, N. T., Petty, A. A., Neumann, T. A., Farrell, S. L., . . . Wimert, J. T.: Surface Height
613            and Sea Ice Freeboard of the Arctic Ocean From ICESat-2: Characteristics and Early Results. *Journal of
614            Geophysical Research: Oceans, 124*, 6942-6959. doi:10.1029/2019JC015486, 2019.

615    Marbouti, M., Praks, J., Antropov, O., Rinne, E., & Leppäranta, M.: A Study of Landfast Ice with Sentinel-1
616        Repeat-Pass Interferometry over the Baltic Sea. *Remote Sensing, 9*. doi:10.3390/rs9080833, 2017.

617    Meyer, F. J., Mahoney, A. R., Eicken, H., Denny, C. L., Druckenmiller, H. C., & Hendricks, S.: Mapping arctic
618        landfast ice extent using L-band synthetic aperture radar interferometry. *Remote Sensing of Environment,*
619        *115*, 3029-3043. doi:https://doi.org/10.1016/j.rse.2011.06.006, 2011.

620    Ocean Networks Canada: Cambridge Bay Underwater Network Ice Profiler Ice Draft Corrected. University of
621        Victoria, Canada, http://www.oceannetworks.ca, 2019. last access: 1 December 2019.

622    Perovich, D. K., Richter-Menge, J. A., Jones, K. F., & Light, B.: Sunlight, water, and ice: Extreme Arctic sea ice
623        melt during the summer of 2007. *Geophysical Research Letters, 35*. doi:10.1029/2008GL034007, 2008.

624    Petty, A. A.; Hutchings, J. K.; Richter-Menge, J. A. & Tschudi, M. A.: Sea ice circulation around the Beaufort Gyre:
625        The changing role of wind forcing and the sea ice state, *Journal of Geophysical Research: Oceans, 121*,
626        3278-3296, 2016.

627    Rosen, P. A.; Hensley, S.; Joughin, I. R.; Li, F. K.; Madsen, S. N.; Rodriguez, E. & Goldstein, R. M.: Synthetic
628        aperture radar interferometry, *Proceedings of the IEEE, 88*, 333-382, 2000.

629    Samsonov, S. V., González, P. J., Tiampo, K. F., & d'Oreye, N.: Modeling of fast ground subsidence observed in
630        southern Saskatchewan Canada during 2008–2011. *Natural Hazards and Earth System Sciences, 14*, 247-
631        257. doi:10.5194/nhess-14-247-2014, 2014.

632    Samsonov, S. V., Lantz, T. C., Kokelj, S. V., & Zhang, Y.: Growth of a young pingo in the Canadian Arctic
633        observed by RADARSAT-2 interferometric satellite radar. *The Cryosphere, 10*, 799, 2016.

634    Steffen, K., & Heinrichs, J.: C-band SAR backscatter characteristics of Arctic sea and land ice during winter.
635        *Atmosphere-Ocean, 39*, 289-299. doi:10.1080/07055900.2001.9649682, 2001.

636    Tilling, R. L., Ridout, A. & Shepherd, A.: Estimating Arctic sea ice thickness and volume using CryoSat-2 radar
637        altimeter data, *Advances in Space Research, 62*, 1203 – 1225, 2018.

638    Tivy, A., Howell, S. E., Alt, B., McCourt, S., Chagnon, R., Crocker, G., . . . Yackel, J. J.: Trends and variability in
639        summer sea ice cover in the Canadian Arctic based on the Canadian Ice Service Digital Archive, 1960–
640        2008 and 1968–2008. *Journal of Geophysical Research: Oceans, 116*.
641        doi:https://doi.org/10.1029/2009JC005855, 2011.

642    Tucker III, W. B., Weatherly, J. W., Eppler, D. T., Farmer, L. D., & Bentley, D. L.: Evidence for rapid thinning of
643        sea ice in the western Arctic Ocean at the end of the 1980s. *Geophysical Research Letters, 28*, 2851-2854.
644        doi:https://doi.org/10.1029/2001GL012967, 2001.

645    Usai, S.: A least squares database approach for SAR interferometric data. *IEEE Transactions on Geoscience and*
646        *Remote Sensing, 41*, 753-760. doi:10.1109/TGRS.2003.810675, 2003.

647    Wadhams, P.: Arctic ice cover, ice thickness and tipping points. *Ambio, 41*, 23-33. doi:10.1007/s13280-011-0222-9,
648        2012.

649    Wegmüller, U., Werner, C., Frey, O., Magnard, C., & Strozzi, T.: Reformulating the Split-Spectrum Method to
650        Facilitate the Estimation and Compensation of the Ionospheric Phase in SAR Interferograms. *Procedia*
651        *Computer Science, 138*, 318-325. doi:https://doi.org/10.1016/j.procs.2018.10.045, 2018.

652    Werner, C., Wegmüller, U., Strozzi, T., & Wiesmann, A.: Gamma SAR and interferometric processing software. *In:*
653        *Proceedings of the ERS-ENVISAT Symposium, Gothenburg, Sweden, 16–20 October 2000.*

654    Zakhvatkina, N., Smirnov, V., & Bychkova, I.: Satellite SAR Data-based Sea Ice Classification: An Overview.
655        *Geosciences, 9*, 152. doi:https://doi.org/10.3390/geosciences9040152, 2019.

656    Zwally, H. J., Yi, D., Kwok, R., & Zhao, Y.: ICESat measurements of sea ice freeboard and estimates of sea ice
657        thickness in the Weddell Sea. *Journal of Geophysical Research: Oceans, 113*. doi:10.1029/2007JC004284,
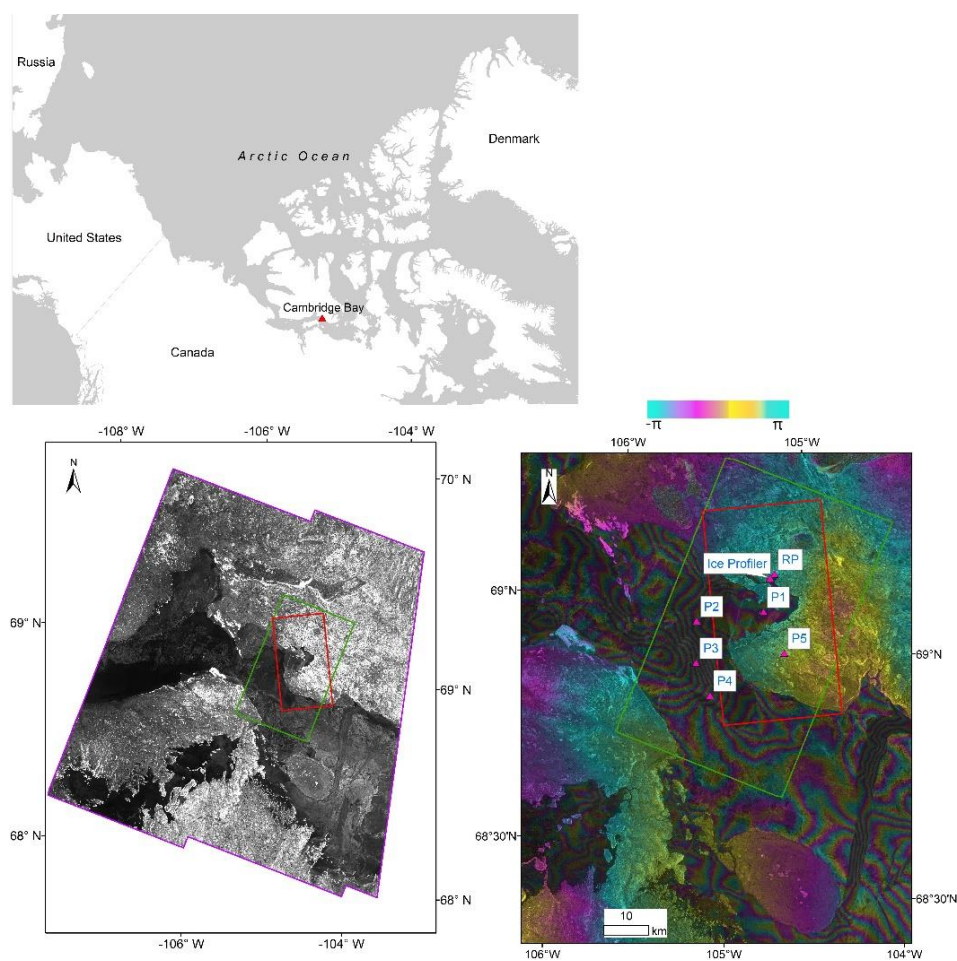658        2008.

659

660

661

662

663



665    Figure 1. Upper left: map of study area showing the Arctic and Cambridge Bay location (the red triangle). Lower left:

666    Cambridge Bay study area covered by Sentinel-1 IW mode (purple line), ALOS-2 HBQR mode (green line) and

667    Radarsat-2 FQ13 mode (red line). The background is a Sentinel-1 image acquired on 2019/3/25. Right: locations of

668 Ice Profiler and InSAR measurement (RP, P1, P2, P3, P4, P5). The background is an example interferogram with clear

669 fringes over the sea ice generated using Sentinel-1 IW mode of HH polarization acquired on 2019/3/25 and 2019/4/6.

670



671
672
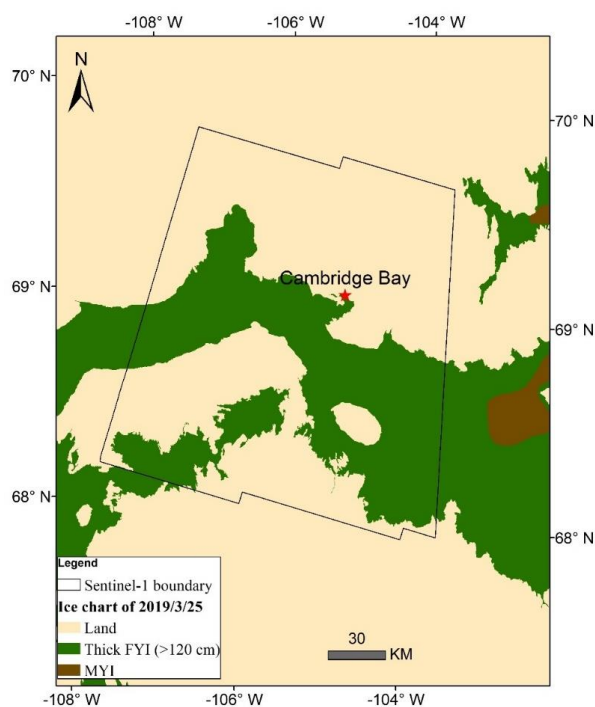
673 Figure 2: Regional ice chart for the study area provided by the Canadian Ice Service Data Archive (CISDA). Chart is

674 valid for March 25, 2019.

675

676

677
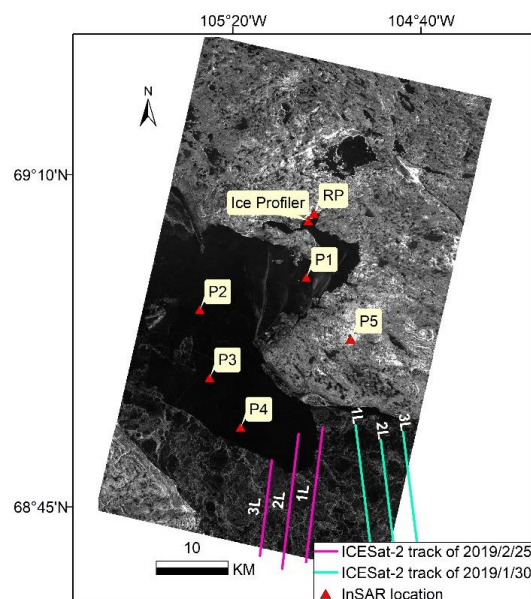
Figure 3. Locations of Ice Profiler, InSAR measurement (RP, P1, P2, P3, P4, P5) and ground tracks of ICESat-2 on a

HH polarized ALOS-2 image from 2019/2/28.

678

679

680

681

682

The Cryosphere
Discussions

Open Access

EGU
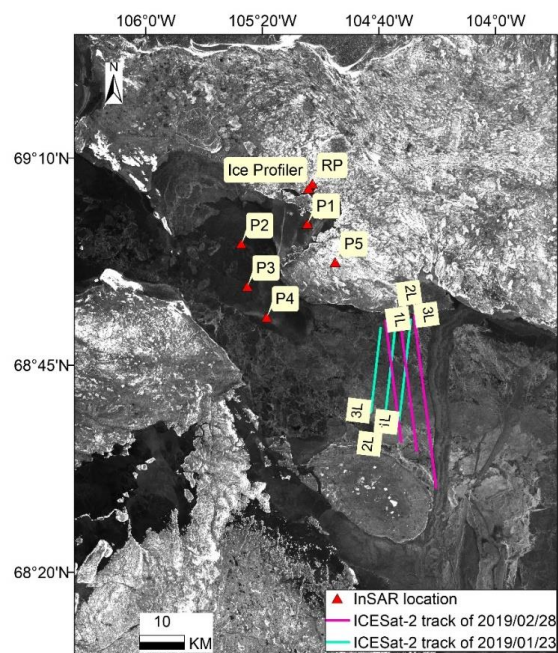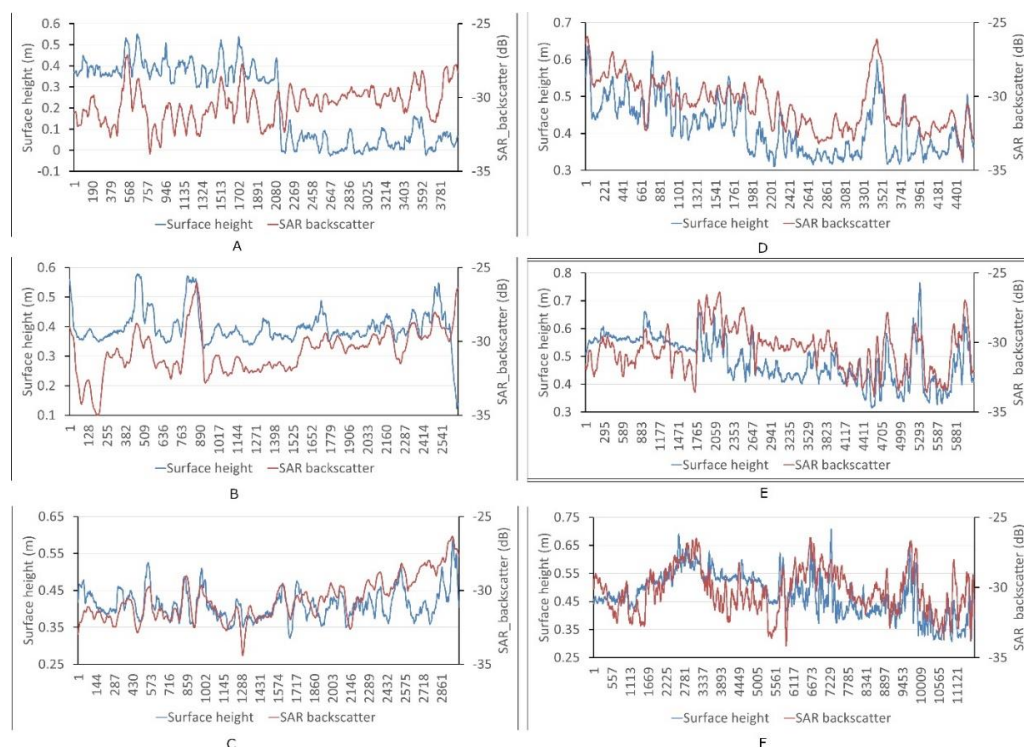
683
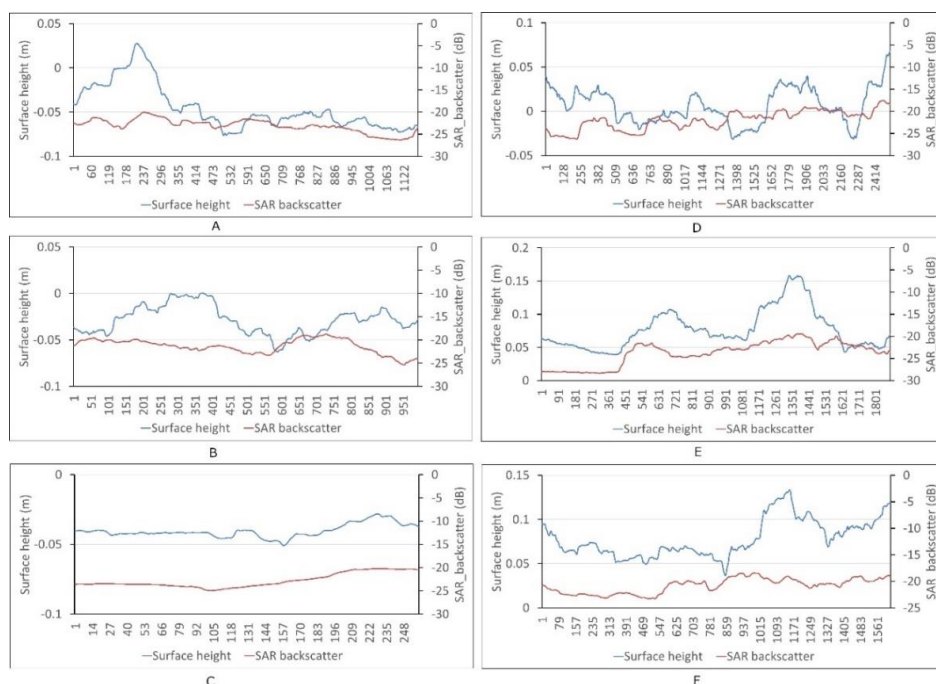
Figure 4. Comparison of surface height measurements from ICESat-2 with SAR backscatter from ALOS-2 (Red line
shows the SAR backscatter and blue line for the surface height). Left: ICESat-2 from 2019/01/30 vs ALOS-2 from
2019/01/31 (values recorded from South to North along the track) ((A), (B) and (C) corresponds to the ground track
of 1L, 2L and 3L); Right: ICESat-2 from 2019/02/25 vs ALOS-2 from 2019/02/28 (values recorded from North to
South along the track) (D, E and F corresponds to the ground track of 1L, 2L and 3L).

684
685
686
687
688

689

690
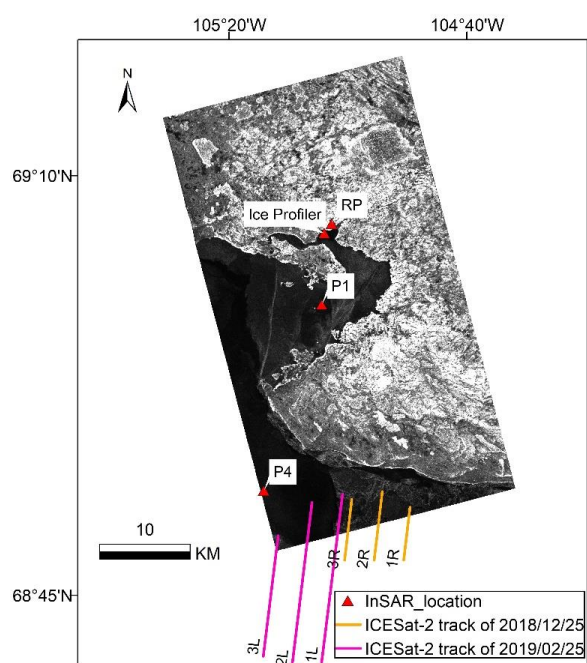
Figure 5. Locations of Ice Profiler, InSAR measurement (RP, P1, P4) and ground tracks of ICESat-2 on an HH polarized Radarsat-2 FQ13 image from 2019/2/8.
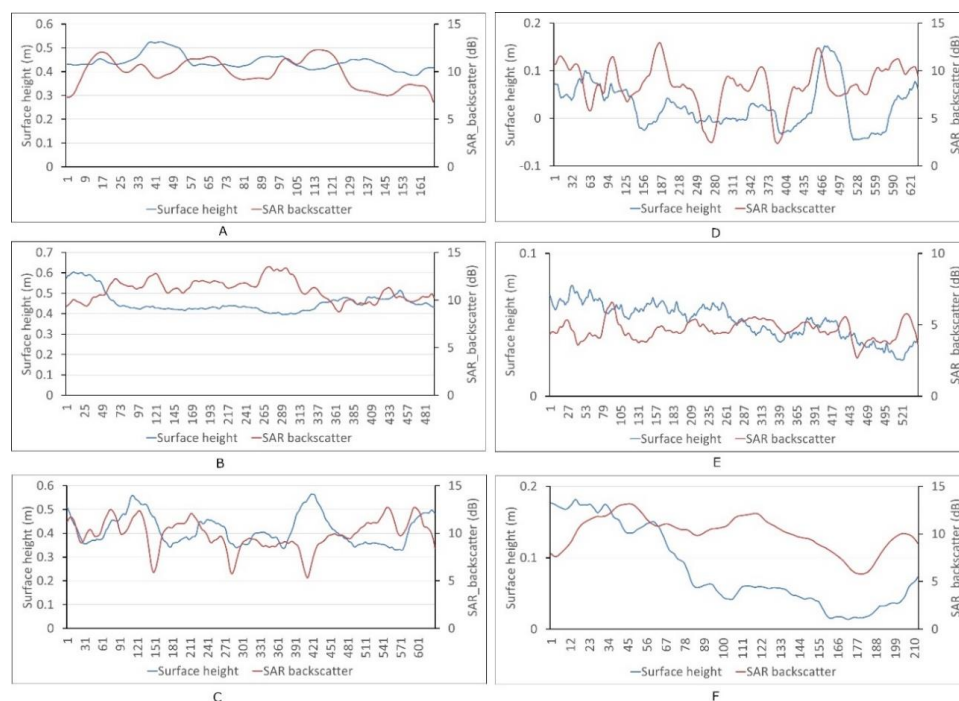
Figure 6. Comparison of surface height measurements from ICESat-2 with SAR backscatter from Radarsat-2 FQ13 (Red line shows the SAR backscatter and blue line for the surface height). Left (A-C): ICESat-2 from 2018/12/25 vs FQ13 from 2018/12/22 (values recorded from North to South along the track); Right (D-F): ICESat-2 from 2019/02/25 vs FQ13 from 2019/02/08 (values recorded from North to South along the track); (A-C). the ground track of 1R-3R; (D-F). the ground track of 1L-3L.

Figure 7. Locations of Ice Profiler, InSAR measurement (RP, P1, P2, P3, P4, P5) and ground tracks of ICESat-2 on a HH polarized Sentinel-1 IW image from 2019/3/1.

Figure 8. Comparison of surface height measurements from ICESat-2 with SAR backscatter from Sentinel-1 IW (Red
line shows the SAR backscatter and blue line for the surface height). Left (A-C): ICESat-2 on 2019/01/23 vs IW on
2019/01/24 (values recorded from North to South along the track); Right (E-F): ICESat-2 on 2019/02/28 vs IW on
2019/03/01 (values recorded from South to North along the track); (A-C). the ground track of 1L-3L; (D-F). the ground
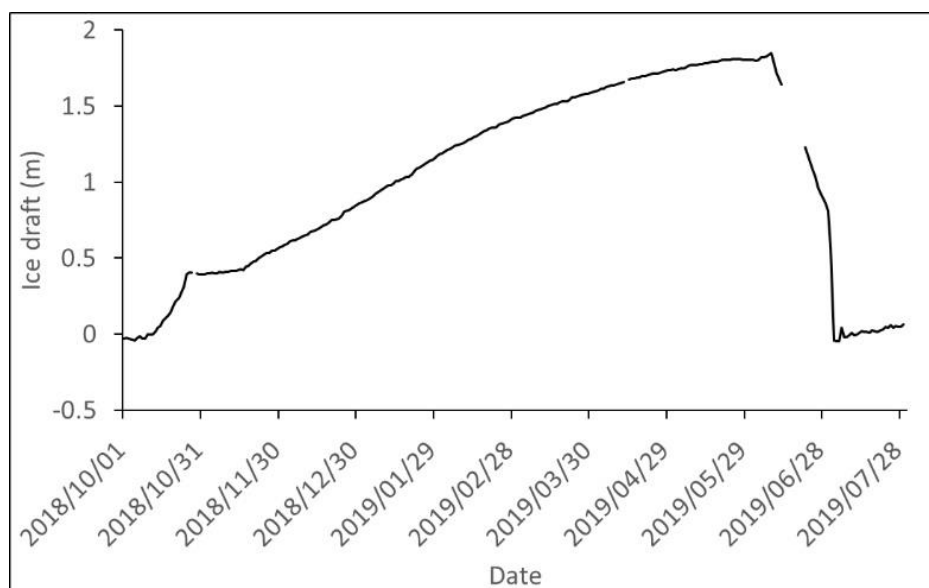track of 1L-3L.
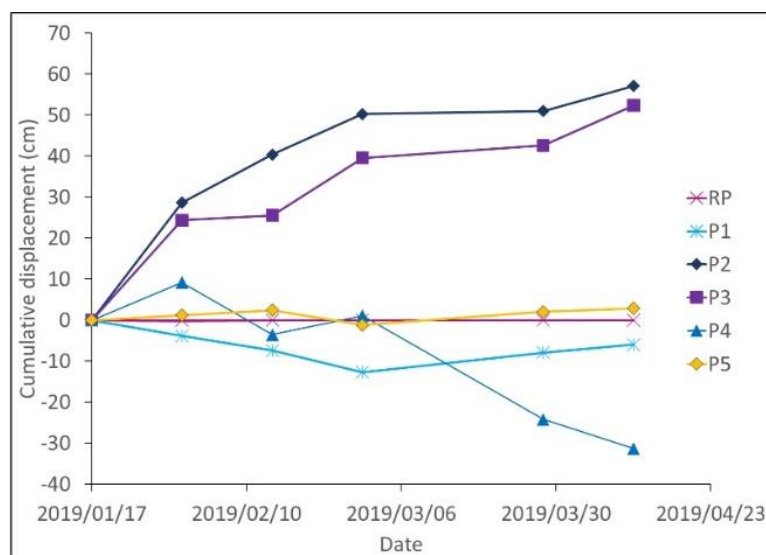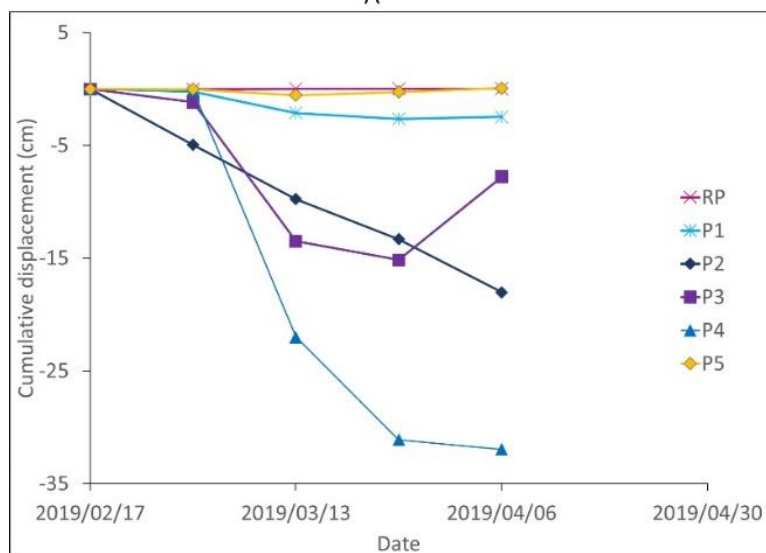
Figure 9. (A). ALOS-2 InSAR cumulative deformation. (B). Sentinel-1 InSAR cumulative deformation. RP is a reference location. P1-P4 are locations over ice, and P5 is a location over land.
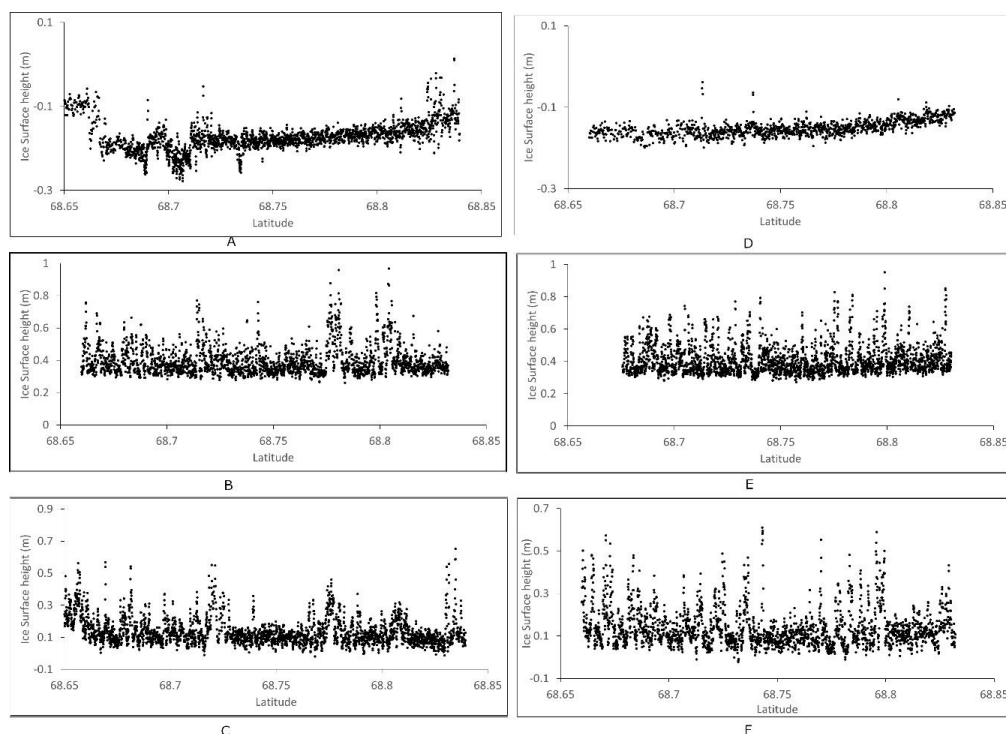
28

719

720  Figure 10. Ice draft changes from a ice profiler located at harbor of Cambridge Bay.
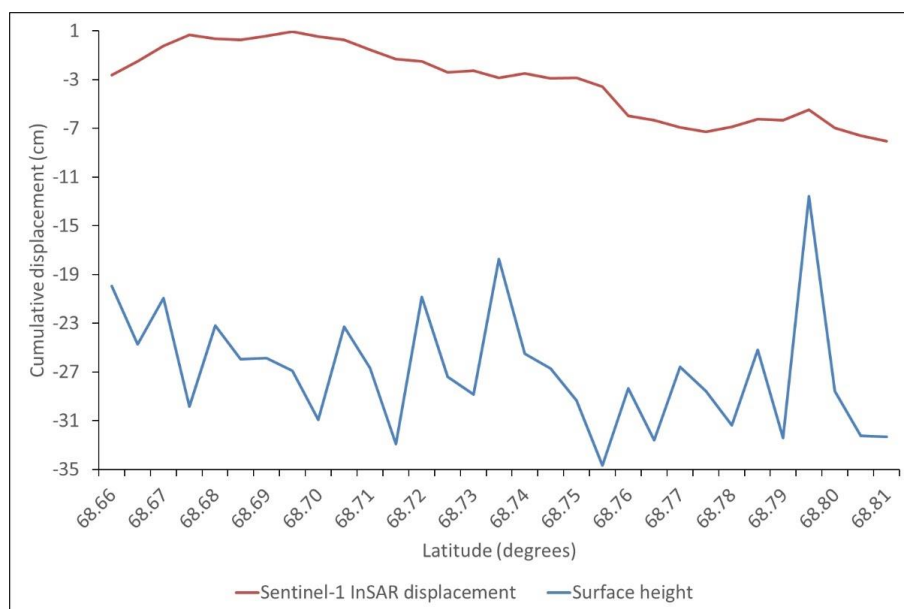
721

722

723

Figure 11. Comparison of surface height measurements from ICESat-2. (A) 1R of 2018/10/24, (B) 2L of 2019/01/23, (C) 1L of 2019/04/24; (D) 2R of 2018/10/24, (E) 3L of 2019/01/23, (F) 2L of 2019/04/24

729



730    Figure 12. Comparison between Sentinel-1 InSAR deformation and surface height changes measured from ICESat-2

731    during January-April 2019 along Line 1 track.

732